Clim. Past Discuss., 8, 1319–1368, 2012
www.clim-past-discuss.net/8/1319/2012/
doi:10.5194/cpd-8-1319-2012


Climate of the Past Discussions



# Influence of LGM boundary conditions on the global water isotope distribution in an atmospheric general circulation model

**T. Tharammal[1,2], A. Paul[1,2,3], U. Merkel[1,3], and D. Noone[4]**

[1]Department of Geosciences, University of Bremen, Bremen, Germany
[2]European Graduate College "Proxies in Earth History" (EUROPROX), University of Bremen, Bremen, Germany
[3]MARUM – Center for Marine Environmental Sciences, University of Bremen, Bremen, Germany
[4]Department of Atmospheric and Oceanic Sciences and Cooperative Institute for Research in Environmental Sciences, University of Colorado, Boulder, USA

Received: 24 March 2012 – Accepted: 5 April 2012 – Published: 18 April 2012

Correspondence to: T. Tharammal (ttharammal@marum.de)

Published by Copernicus Publications on behalf of the European Geosciences Union.







## Abstract

A series of experiments was conducted using a water isotope tracers-enabled atmospheric general circulation model (Community Atmosphere Model version 3.0, CAM3.0-Iso), by changing the individual boundary conditions (greenhouse gases, ice sheet albedo and topography, sea-surface temperature) each at a time to Last Glacial Maximum (LGM) values. In addition, a combined simulation with all the boundary conditions being set to LGM values was carried out. A pre-industrial (PI) simulation with boundary conditions taken according to the PMIP2 (Paleoclimate Modelling Intercomparison Project) protocol was performed as the control experiment. The experiments were designed in order to analyze the temporal and spatial variations of the oxygen isotopic composition of precipitation ($\delta^{18}O_{precip}$) in response to individual climate factors. The change in topography (due to the change in land-ice cover) played a significant role in reducing the surface temperature and $\delta^{18}O_{precip}$ over North America. Exposed shelf areas and the ice sheet albedo reduced the Northern Hemisphere surface temperature and $\delta^{18}O_{precip}$ further. A global mean cooling of 4.1 °C was simulated with combined LGM boundary conditions compared to the control simulation, which was in agreement with previous experiments using the fully coupled Community Climate System Model (CCSM3). Large reductions in $\delta^{18}O_{precip}$ over the LGM ice sheets were highly correlated with the temperature decrease over them. The SST and ice sheet topography changes were found to be responsible for most of the changes in the climate and hence the $\delta^{18}O_{precip}$ distribution among the simulations.

## 1 Introduction

The Last Glacial Maximum (LGM, about 19 000–23 000 yr before present) is the largest change in climate during recent geological times, that is the last 100 000 yr. A strong cooling in both hemispheres is recorded in the proxy records from Greenland (Dahl-Jensen et al., 1998) and Antarctica (Stenni et al., 2001). During the LGM, a large





CPD
8, 1319–1368, 2012



portion of North America and Northern Eurasia was covered by ice sheets, hence the sea level was reduced by about 120 m (Fairbanks, 1989; Lambeck and Chappell, 2001). The newly exposed land areas increased the surface albedo. Differences in vegetation and soil type also impacted the surface albedo. The Laurentide Ice Sheet covering most of Canada and a large portion of the Northern United States had a first-order impact on the large-scale atmospheric circulation in the Northern Hemisphere via topographic and thermal forcing as demonstrated in global circulation models (Manabe and Broccoli, 1985). A reduced atmospheric concentration of $CO_2$ (185 ppmv, Petit et al., 1999) compared to the preindustrial (PI, approximately 1800 AD) value of 280 ppmv is also expected to influence the global temperature and affect the distribution of the oxygen isotopic composition of precipitation.

A temperature-dependent isotopic fractionation occurs during any phase transition because of the differences in the saturation vapor pressures between the isotopic forms of the water molecule ($H_2{}^{16}O$, $H_2{}^{18}O$, HDO). This causes the ratios of the heavier to lighter isotopes in the different reservoirs of the hydrological cycle to vary depending on the atmospheric conditions.

The ratios of the heavy to the light isotopes are denoted by so-called $\delta$ values, given as $\delta^{18}O=(R_{SAMPLE}/R_{VSMOW}-1)\times 1000‰$, where $R$ is the ratio of the heavier oxygen isotope $^{18}O$, and the lighter isotope $^{16}O$. Furthermore, $R_{SAMPLE}$ and $R_{VSMOW} = 2.0052\times 10^{-3}‰$ are the isotopic concentrations of the sample and of VSMOW (Vienna Standard Mean Ocean Water), respectively.

At high latitudes, $\delta^{18}O$ in precipitation ($\delta^{18}O_{precip}$) is strongly correlated with the local surface temperature (temperature effect). In the tropics, $\delta^{18}O_{precip}$ is closely related to the precipitation amount (amount effect, Dansgaard, 1964). Thus, highly depleted stable isotope concentrations are observed during time periods of intense precipitation (Rozanski et al., 1993). The long-term variations in the $\delta^{18}O_{precip}$ over the mid- and high latitudes are observed to follow the long term variations of surface air temperature, the factor of proportionality being around $0.6‰\,^{\circ}C^{-1}$ (Rozanski et al., 1993). For temperatures below 14 °C, the annual-mean $\delta^{18}O$ is closely related to





CPD
8, 1319–1368, 2012



the annual-mean surface temperature $T$ as $\delta^{18}O$=0.62‰°C$^{-1}$ $T$ −15.25‰ (Dansgaard et al., 1973; Johnsen et al., 1989). Modeling studies have attempted to see whether this present-day temperature-$\delta^{18}O_{precip}$ relationship could be extended to climates that differ starkly from the present. Stable water isotopes have been included in the hydrological cycle of various global atmospheric models, namely, GISS (Jouzel et al., 1987), ECHAM (Hoffmann et al., 1998), CAM2.0 (Lee et al., 2007), CAM 3.0 (Noone and Sturm, 2009), LMDZ (Bony et al., 2008), MUGCM (Noone and Simmonds, 2002) and the atmosphere-ocean coupled model HadCM3 (Tindall et al., 2009). These models were successfully used for simulating the present and paleoclimatic distributions of the stable isotopes in the global hydrological cycle. Lee et al. (2008) found that the apparent temporal slope (relationship of $\delta^{18}O_{precip}$ with surface temperature in a given geographical location through different time-varying climates) over Eastern Antarctica is half of the observed spatial slope (latitudinal relationship) for the LGM and that the value of the temporal slope is related to the temperature decrease over the Southern Ocean, with an experiment using two different sea-surface temperature (SST) distributions. Charles et al. (1994) found that changes in moisture transport and source regions for Greenland at the LGM may have produced an isotopic response independently of temperature changes. Masson-Delmotte et al. (2006) showed that a major part of the Greenland and Antarctic coolings of the GCM simulations is caused by the prescribed local elevation increase due to ice sheets at the LGM. Werner et al. (2000) found an increased seasonality in the annual cycle of precipitation over Greenland during the LGM, but not over Antarctica. These studies point to the importance of understanding the influence of the various forcing factors on the isotope distribution. Following Broccoli and Manabe (1987b), we used an atmospheric general circulation model to test the effect of the individual boundary conditions on the last glacial maximum climate in terms of surface temperature, precipitation and $\delta^{18}O_{precip}$. This is the first attempt to study the sensitivity of an isotope-enabled model to individual LGM boundary conditions.





CPD
8, 1319–1368, 2012



## 2 The model and experiments

### 2.1 The model

We used the NCAR Community Atmosphere Model CAM3.0 (Collins et al., 2006) with a water isotopes scheme included, hereafter referred to as CAM3.0-Iso. The isotopic version of CAM is based on the earlier isotopic scheme of Noone and Simmonds (2002), but includes a more sophisticated treatment of surface exchange and cloud processes to make use of the multiple water phases predicted by CAM (Noone, 2003, 2006; Noone and Sturm, 2009; Sturm et al., 2010). The spatial resolution employed in our experiments corresponds to a spectral truncation of T31 and 26 hybrid levels in the vertical. The related Gaussian grid has a spatial resolution of 3.75° × 3.75° (48 grid points in latitude and 96 grid points in longitude). Each atmospheric grid box in CAM3.0 contains a specific fraction of land, ice, or ocean. The ability of CAM3.0 to efficiently simulate the global hydrological cycle is detailed in Hack et al. (2006).

CAM is coupled to the Community Land Model, CLM (Bonan et al., 2002), which uses the same grid as the atmospheric model. CLM includes different forms of land surface types within each grid cell, namely lakes, glaciers, wetlands and up to 16 land plant functional types (PFTs) that can include a bare soil (Dickinson et al., 2006). For the calculation of isotope ratios over land a simple bucket model (Manabe, 1969) is used, which does not differentiate between evaporation and river runoff or different soil types (Deardorff, 1977; Noone and Simmonds, 2002). The isotope ratios over land do not take into account the fractionation during evapo-transpiration or the effect of different vegetation types.

A thermodynamic sea-ice model (CSIM) represents the ice component of the model. CSIM computes the surface fluxes when used with prescribed SST. It further predicts snow depth, brine pockets, internal shortwave radiative transfer, surface albedo, ice-atmosphere drag and surface exchange fluxes without the use of a flux coupler (Collins et al., 2006).





CPD
8, 1319–1368, 2012



The stable isotopes of water in the hydrological cycle of the CAM3.0-Iso are transported through the atmosphere and the ground by the same processes (advection, moist convection, evapo-transpiration etc.) used to transport normal water (Noone and Sturm, 2009). The isotopes of hydrogen are also included in the model, but were not considered for analysis in this study. The isotopic fractionation occurs with every phase change of the water species in the model hydrology. CAM3.0-Iso uses a semi-Lagrangian formulation for the water vapor and tracer transport (Williamson and Rasch, 1993; Williamson and Olson, 1994), which has been found to be sufficiently accurate for conserving isotopic ratios during advection to low temperature environments.

## 2.2 Experiments and boundary conditions

A series of experiments was carried out by changing the individual boundary conditions (greenhouse gases (GHG), albedo, topography, SST along with sea-ice concentration, orbital parameters) each at a time to LGM values. In addition, a combined simulation with all the boundary conditions set to LGM values was carried out (LGM-combined hereafter). A pre-industrial (PI, approximately 1800 AD) simulation with boundary conditions according to the PMIP2 (Paleoclimate Modelling Intercomparison Project) protocol (Braconnot et al., 2007) served as the control run. The extent and the height of the ice-sheets at the LGM were taken from the ICE-5G ice-sheet topography (Peltier, 2004). The SST datasets for the pre-industrial and LGM period were derived from previous fully-coupled CCSM3 simulations (Merkel et al., 2010). According to Craig and Gordon (1965), the surface ocean oxygen isotopic ratio was set to the same constant initial value of 0.5 ‰, and the surface ocean hydrogen isotope ratio was set to 4 ‰ for all the experiments. The pre-industrial SST data was prescribed for each of the simulations in the series, with the exception of the LGM-SST and LGM-combined simulations, where a climatology derived from the corresponding fully-coupled LGM simulation was used. The boundary conditions for each experiment are listed in Tables 1 and 2. The orbital parameters for the pre-industrial control, GHG, albedo and topography simulations were prescribed to the reference values of 1950 AD, while the orbital parameters





CPD
8, 1319–1368, 2012



for the orbital only and for the LGM-combined simulation were set to the 21 ka BP values (Berger, 1978). In the GHG experiment, only the atmospheric greenhouse gas concentrations were reduced to the LGM concentrations. The albedo experiment was conducted by replacing the land ice cover of the PI simulation with LGM values, thereby changing the surface albedo to that of the LGM. The topography experiment was conducted by taking into account the change in topography and the lowering of sea level during the LGM by 120 m (Fairbanks, 1989). All simulations were integrated for 35 model years, and the last 10 yr of each simulation were used for analysis.

The CCSM3.0 and CAM3.0 models have been shown to successfully reproduce the observed distributions of surface temperature and total precipitation as described in Otto-Bliesner et al. (2006b) and Hack et al. (2006). The annual and seasonal distribution of $\delta^{18}O_{precip}$ for the PI control climate is shown in Fig. 1. The CAM3.0-Iso model captures well the main features of the annual-mean $\delta^{18}O_{precip}$ when compared to the Global Network of Isotopes in precipitation (GNIP, IAEA/WMO, 2006) database (not shown).

## 3 Regional mean responses in surface temperature, precipitation and $\delta^{18}O_{precip}$

The impact of the glacial boundary conditions on the surface temperature and precipitation is summarized in Tables 3 and 4, respectively. The annual-mean cooling in the surface temperature was 4.1 °C in our LGM-combined experiment with respect to the PI experiment, while the reduction of annual-mean precipitation was 0.22 mm day$^{-1}$, in good agreement with the previous simulations using CCSM3 (Otto-Bliesner et al., 2006a). The SST experiment brought about a global mean cooling of 2.79 °C. The cooling of 0.18 °C and 0.14 °C in the albedo and GHG experiments, respectively, was comparatively small. The ice-sheet topography led to a reduction of the global mean surface temperature by 0.44 °C. Note that the change in topography caused a mean cooling of 0.59 °C in the Northern Hemisphere (NH), while in the Southern Hemisphere (SH) the magnitude of the induced cooling was only 0.27 °C. The global mean cooling





CPD
8, 1319–1368, 2012



in the orbital experiment was the weakest among all the simulations with a magnitude of 0.02 °C. A slight increase of precipitation was simulated in the GHG experiment (0.03 mm day$^{-1}$) in the global mean, but it was accompanied by a reduction in precipitation over land (Table 4). The precipitation in the tropics shows the strongest response in the SST experiment and was reduced in all the experiments except for the GHG simulation.

The annual-mean $\delta^{18}O_{precip}$ and the difference from the control experiment for the North American and Eurasian ice sheets, Greenland, North Africa, South Africa, Northern and Southern South America and Antarctica for each experiment are given in Table 5 (geographical regions defined by appropriate latitude-longitude grid boxes). Over North Africa a strong enrichment was simulated in all the experiments compared to the control experiment, with the maximum response in the LGM-combined experiment (1.57 ‰), where the albedo and GHG experiments produced an enrichment of around 1 ‰, while the topographic experiment yielded the smallest change of 0.22 ‰.

In South Africa, only a small depletion was simulated in all experiments. The maximum depletion was found in the SST and LGM experiments (0.89 ‰ and 0.86 ‰, respectively), while the GHG, albedo and topographic experiments resulted in smaller changes. Over Greenland, the mean value of $\delta^{18}O_{precip}$ was −22.3 ‰ in the LGM-combined experiment, which was 2.21 ‰ more depleted than in the control experiment. The SST experiment gave the largest signal among all experiments with a decrease of 2.6 ‰ over Greenland. The other experiments showed only small changes in the mean value. The region covered by the Eurasian ice sheet experienced a depletion of 5.9 ‰ in the LGM-combined experiment in comparison with the PI experiment, whereas the topography and SST simulations led to a reduction by 2.11 ‰ and 2.7 ‰, respectively. The changes in the GHG, orbital, and albedo experiments were negligible. The strongest response (a reduction of 10.3 ‰) was simulated in the LGM-combined experiment over the Laurentide ice-sheet where the topography change reduced the concentration by 3.3 ‰. Over Antarctica, a uniform depletion was simulated,





CPD
8, 1319–1368, 2012



with an area-averaged anomaly of 2.2‰ in the LGM-combined and 1.2‰ in the SST experiment.

## 4 Zonal mean response of surface temperature, precipitation and $\delta^{18}O_{precip}$

### 4.1 Surface temperature

The differences between the zonal averages of surface temperature of the individual experiments and the PI control experiment are shown in Fig. 2a. The zonal averages in the orbital, GHG and albedo experiments did not deviate from the control experiment in the tropics and the Southern Hemisphere. In the Northern Hemisphere the surface temperature was reduced by 1 °C to 1.5 °C in the albedo experiment, while the orbital and GHG simulations showed very small variation in the northern polar region. In the topography experiment, the temperature was lower by 1 °C to 9 °C in the high latitudes of the Southern Hemisphere, while the subtropics and tropics showed comparatively small variations. In the Northern Hemisphere, surface temperature was reduced by 2 °C to 3 °C in response to the topography changes. In the SST experiment, the surface temperature was reduced by 3 °C in the tropical regions; furthermore a sharp gradient was seen in both hemispheres, with a cooling of 8 °C in the subtropics and 4 °C in the polar regions. The LGM-combined simulation followed the pattern of the SST experiment, except for the latitude range north of 30° N, where the LGM-combined experiment simulated a further cooling of 3 °C compared to the SST experiment. Thus, the ice sheet/topography and SST-induced cooling were found to be responsible for most of the lowering of surface temperature north of 30° N. The southern high latitudes showed a stronger cooling than the northern counterparts by 4 °C to 5 °C.

### 4.2 Total precipitation

Figure 2b shows the differences in the zonal means of the total precipitation in the different experiments with respect to the PI control run. A reduction of precipitation was





CPD
8, 1319–1368, 2012



simulated in the zonal averages of all the experiments. Precipitation was increased at 30° S–60° S and also slightly in the tropical regions in the GHG experiment. The zonal average of precipitation in the northern polar regions was unaffected by GHG reduction. Precipitation was reduced near the equator and 60° N in the albedo experiment while the change in orbital parameters did not change the precipitation noticeably. Precipitation in the topography experiment did not deviate considerably from the PI precipitation, but a dip in the precipitation amount was simulated over the elevated ice sheet topography. This could be due to a southward shift of rainbearing frontal zones. The SST and LGM-combined experiments simulated the highest deviations from the PI precipitation amount. The precipitation amount in these experiments was reduced by 0.6 mm day$^{-1}$ from 50° S to 80° S and by 0.4 mm day$^{-1}$ near the equator. In the Northern Hemisphere subtropics and high latitudes the SST and LGM-combined experiments showed a reduction of precipitation by 0.2 mm day$^{-1}$, while the LGM-combined experiment simulated a slight increase of precipitation at 30° N compared to PI.

### 4.3 $\delta^{18}$O in precipitation

Figure 2c shows the difference of zonal means of $\delta^{18}O_{precip}$ of each experiment from the control run. The orbital, GHG, and albedo experiments did not simulate major variations from the control run in the Southern Hemisphere, while depleted values were noted in the northern high latitudes. Also, a slight enrichment in the tropical regions compared to the control climate was simulated by these experiments. The topography changes brought about a depletion of $\delta^{18}O_{precip}$ concentration by 1 ‰ to 2 ‰ in the northern high latitudes. The southern high latitudes also showed a depletion of $\delta^{18}O_{precip}$ concentration by 2 ‰ to 3 ‰ due to the LGM topography, but from 60° S to 20° N no anomalies from the control climate were found. The LGM-combined experiment had a strong response in Southern Hemisphere mid-latitudes, with a depletion of 4 ‰ in comparison with the control run. Both polar regions simulated a depletion of 2 ‰ to 3 ‰ compared to the PI, while in the equatorial region the values were close to the PI concentration. The SST experiment followed the same pattern as the LGM-combined





CPD
8, 1319–1368, 2012



experiment in the tropics and equatorial regions. But at the higher latitudes the effect of the ice-sheet albedo and topography in the LGM-combined experiment led to a more depleted concentration of $\delta^{18}O_{precip}$ as compared to the SST run.

## 5 Annual mean spatial response to the different forcings

### 5.1 GHG

The experiment forced with the reduced LGM GHG concentrations shows (Fig. 3a) that there was a uniform reduction of surface temperature, especially over the Northern Hemisphere landmass, and only little response over the Southern Hemisphere. The range of cooling was from about 0.5 °C to 2 °C. Globally, the $\delta^{18}O_{precip}$ values changed in the range from −3‰ to 4‰ compared to the PI simulation (Fig. 4a). The strongest response of $\delta^{18}O_{precip}$ was found over Africa, with positive values of 0.5‰ to 4‰ over Northern Africa, but also over Australia. The precipitation rate in the GHG experiment did not differ substantially with respect to the control simulation (Fig. 5a), with the response varying between $-0.8\,mm\,day^{-1}$ to $1\,mm\,day^{-1}$. At 40° S to 60° S, a rather small reduction of the precipitation rate in comparison with the control experiment was noted. A slight positive anomaly of $0.1\,mm\,day^{-1}$ to $0.4\,mm\,day^{-1}$ was simulated in the tropics.

### 5.2 Ice-sheet albedo

The presence of ice sheets increases the albedo of the ice-covered grid cells. The effect of the albedo change was seen predominantly in the Northern Hemisphere with a cooling of 1 °C to 5 °C (Fig. 3b). $\delta^{18}O_{precip}$ followed the temperature pattern over the Northern Hemisphere ice sheets, with a reduction of 1.5‰ to 2‰ compared to PI values (Fig. 4b). In addition, $\delta^{18}O_{precip}$ values showed a +2‰ difference from PI over Northern Africa.

The precipitation rate showed weak anomalies of $-0.8\,mm\,day^{-1}$ to $1.0\,mm\,day^{-1}$ with respect to the PI control simulation (Fig. 5b). Over North America and Greenland





CPD
8, 1319–1368, 2012



the precipitation was 0.2 mm day$^{-1}$ to 0.6 mm day$^{-1}$ lower than that of the control simulation.

### 5.3 Topography

The ice-sheet topography experiment yielded regional cooling in the locations of elevated orography during the LGM (Fig. 3c). The large difference in topography of the LGM played a decisive role in the LGM climate, as the elevation change is at about 2 km over the North American and Eurasian ice sheets. The surface temperature was lower by −15 °C than that of the PI value over North America, and a 3 °C to 5 °C cooling over both the North and South Poles was found.

The $\delta^{18}O_{precip}$ got depleted by 5 ‰ to 15 ‰ over the ice sheets (Fig. 4c). Depletion by 1 ‰ was also seen over the Asian continent. In contrast, an enrichment of $\delta^{18}O_{precip}$ by 0.5 ‰ to 1 ‰ was simulated over the desert region in North Africa, while over the North West coastal areas of Africa, a negative anomaly was simulated in comparison with the control run.

The response in the annual-mean precipitation to the topography change (Fig. 5c) was stronger in comparison with the GHG and albedo experiments (Fig. 5a, b). The precipitation rate was reduced over the elevated topography in the Northern Hemisphere, while southern high latitudes did not show any pronounced change in precipitation.

### 5.4 Orbital parameters

The effect of changes in the orbital parameters on the simulated climate and $\delta^{18}O_{precip}$ was small, with the visible changes seen mostly as a cooling of around 1 °C over parts of North America and Europe (Fig. 3d). Figure 4d illustrates the response of $\delta^{18}O_{precip}$ to the orbital forcing during the LGM. The $\delta^{18}O_{precip}$ values over North Africa increased by 1 ‰ to 2 ‰. Similar to the minimal surface temperature response, small





CPD
8, 1319–1368, 2012



scale changes were seen in the precipitation response with an increase in the range of 0.1 mm day$^{-1}$ to 1 mm day$^{-1}$ over the globe (Fig. 5d).

### 5.5 SST

The response of annual-mean surface temperature in the glacial SST experiment is shown in Fig. 3e. Over the North Atlantic Ocean and the Southern Ocean south of 30° S, the surface temperatures were considerably reduced compared to the PI experiment. The surface temperature over the northern high latitudes and polar regions was reduced by more than 12 °C. The $\delta^{18}O_{precip}$ was more depleted over the high latitudes and more enriched over the tropics and Central Antarctica (Fig. 4e). $\delta^{18}O_{precip}$ was depleted over South Africa in comparison with the PI annual mean values by 2 ‰. The strongest response in precipitation was found in the tropics and exhibits both positive and negative anomalies.

### 5.6 LGM – combined

Strong anomalies in the temperature (Fig. 3f) and $\delta^{18}O_{precip}$ (Fig. 4f) fields were found especially in high latitudes. A strong cooling in surface temperature during the LGM and a similar pattern of reduction in $\delta^{18}O_{precip}$ over the expanded ice sheets were simulated, which follows from the colder and drier climate over them. The response of $\delta^{18}O_{precip}$ to the LGM-combined boundary conditions (Fig. 4f) showed an enrichment in $\delta^{18}O_{precip}$ by 0.5 ‰ to 2 ‰ over the African continent and over the Indian subcontinent compared to the control simulation.

The precipitation rate in the LGM-combined run (Fig. 5f) showed anomalies of −3 mm day$^{-1}$ to +3.5 mm day$^{-1}$ in comparison with the control run. The precipitation rate was reduced in the Northern Hemisphere compared to the PI simulation by 1 mm day$^{-1}$ to 2 mm day$^{-1}$. The introduction of ice sheets brought about the drying up of the atmosphere and consequently less precipitation. The western part of the North American land mass and part of the ocean regions showed a local maximum of





CPD
8, 1319–1368, 2012



precipitation compared to the control run with a difference in the range from 1 mm day$^{-1}$ to 2 mm day$^{-1}$. The positive and negative anomalies in precipitation simulated over the tropics were similar to the response modeled in the LGM-SST experiment, which points to a local response in precipitation to the changes in SST.

### 5.7 The relationship of $\delta^{18}O_{precip}$ to surface temperature and precipitation

In order to understand the relationship between annual mean $\delta^{18}O_{precip}$ and surface temperature under different climate states, a simple linear regression analysis is used to calculate the spatial slopes over Greenland and Antarctica (Fig. 6a–d). Modelled annual mean values of surface temperature and $\delta^{18}O_{precip}$ for all model grid boxes in inner Greenland and Antarctica were used for the calculation. Over Greenland, the PI control run gave a relationship of $\delta^{18}O_{precip}=0.63T-10.8$‰ (Fig. 6a, $T$ in °C). The SST (slope 0.58 ‰ °C$^{-1}$), topography (slope 0.60 ‰ °C$^{-1}$) (not shown) and LGM-combined experiments (Fig. 6b) deviated notably from the PI relationship. For the LGM-combined experiment the relationship was found to be $\delta^{18}O_{precip}=0.54T-7.6$‰ ($T$ in °C).

Over Antarctica, the control simulation simulated a relationship of $\delta^{18}O_{precip}=0.54T-11.94$‰ (Fig. 6c, $T$ in °C). Changes with respect to the control run were simulated in the topography ($\delta^{18}O_{precip}=0.48T-13.57$‰, $T$ in °C), SST ($\delta^{18}O_{precip}=0.48T-12.30$‰, $T$ in °C), and LGM-combined ($\delta^{18}O_{precip}=0.45T-12.60$‰, $T$ in °C) experiments (Fig. 6d). The albedo and GHG experiments yielded slopes that are identical to those in the control simulation over both Greenland and Antarctica (not shown).

Figure 6e,f show the relationship between the annual-mean precipitation and $\delta^{18}O_{precip}$, i.e., the amount effect over the tropics (from 20° S to 20° N) for the PI control and LGM-combined simulations. The $\delta^{18}O_{precip}$ got more depleted with an increase in the amount of precipitation in all the experiments. The modelled relation between total precipitation ($P$) and $\delta^{18}O_{precip}$ for the control experiment was





CPD
8, 1319–1368, 2012



$\delta^{18}O_{precip} = -0.51 \times P - 2.66$‰ (slope in ‰ per mm day$^{-1}$). The GHG, albedo, topography and orbital experiments produced small-scale deviations in the range of 0.01–0.02‰ per mm day$^{-1}$ (not shown) from the slope obtained for the control run. The LGM-combined and SST experiments differed from the PI relationship, with slopes of −0.60 and −0.58‰ per mm day$^{-1}$, respectively.

## 6 Seasonal signals in the sensitivity experiments

In order to address the seasonal variations of the climate variables, the difference between boreal summer (June–August, JJA) and boreal winter (December–February, DJF), JJA minus DJF, for the surface temperature, $\delta^{18}O_{precip}$ and precipitation are calculated for the PI and LGM-combined simulations.

### 6.1 Seasonal cycle in control and LGM-combined climates

#### 6.1.1 Seasonal cycle in the PI control climate

The "JJA minus DJF" difference of the PI simulation is shown in Fig. 7. The boreal summer (JJA) temperatures yielded a strong contrast of 16 °C to 35 °C to the winter season over the northern latitude continents, the temperature over Eurasia showed a difference of 32 °C from the winter and 8 °C to 20 °C over Greenland. The temperature in the tropics showed a slight cooling of 2 °C in the boreal summer compared to the DJF season. Over the Southern Ocean, a seasonal contrast of 16 °C to 32 °C was simulated.

$\delta^{18}O_{precip}$ was enriched by 2‰ to 14‰ in the boreal summer compared to the winter season in the Northern Hemisphere notably over the ice-sheets and Eurasia, while over Greenland a seasonal signal was seen only in the north where a summer enrichment of 2‰ to 4‰ was simulated. The maximum value of 14‰ was found over Eastern Eurasia and Eastern North America. There was an enrichment of 6‰ to 8‰ over the 0–30 °S latitudes, while it was depleted in the Northern Hemisphere counterparts





CPD
8, 1319–1368, 2012



in the JJA season. The summer precipitation at 0–20° N was higher by 8 mm day$^{-1}$ to 15 mm day$^{-1}$ compared to the winter season. South of the equator, the seasonal contrast in precipitation points to more precipitation during the DJF than during the JJA season.

### 6.1.2 Seasonal cycle in the LGM- combined climate

The "JJA minus DJF" difference of the LGM-combined simulation is illustrated in Fig. 8.

The surface temperature over the Northern Hemisphere high latitudes in boreal summer (JJA) was higher by 30 °C than in the winter (DJF) months. The surface temperatures over the southern mid-to-high latitudes were reduced by 8 °C to 16 °C during JJA. The $\delta^{18}O_{precip}$ was enriched over the Laurentide and Eurasian ice sheets by around 14 ‰ in the boreal summer. The amplitude of the seasonal cycle of surface temperature over the northern latitudes (> 30° N), especially over Greenland, Eurasia and Laurentide ice sheets in the LGM climate was stronger than the PI climate. For $\delta^{18}O_{precip}$, the strength of the seasonal cycle in the control climate was found to be larger over the Laurentide ice-sheets, while over Eurasia the LGM seasonal amplitude was stronger. Seasonality of precipitation in the LGM climate was weaker than in the control climate over the whole globe. A distinct seasonality in the isotope distribution was absent in Central Greenland, which also was absent in the control simulation, while a slight enrichment was simulated during the JJA season in the south.

## 6.2 Seasonal response in the experiments in comparison with PI

The difference between the seasons of each experiment from those of the control run was calculated to assess the effect of the individual boundary conditions on the seasonal distribution of $\delta^{18}O_{precip}$. The summer and the winter anomalies of $\delta^{18}O_{precip}$ are shown in Figs. 9 and 10, respectively.





CPD
8, 1319–1368, 2012



### 6.2.1 GHG

The $\delta^{18}O_{precip}$ concentration in the GHG experiment was depleted by 0.5‰ to 2‰ over the Northern Hemisphere land-masses in the DJF season when compared to the PI boreal winter (Fig. 9a), along with a reduction in surface temperature (not shown). Over Central Africa and Australia the $\delta^{18}O_{precip}$ was enriched.

In JJA (Fig. 10a) the $\delta^{18}O_{precip}$ was enriched over Antarctica where the surface temperature was reduced compared to the PI boreal summer. An enrichment over North Africa was seen which corresponds to decreased precipitation while the concentration was depleted over the other continents in response to the LGM GHG concentrations.

### 6.2.2 Albedo

$\delta^{18}O_{precip}$ was depleted over the Laurentide ice sheets and Eurasia with the reduction in surface temperature when compared to PI boreal winter (Fig. 9b). The $\delta^{18}O_{precip}$ was depleted over the Saharan desert during DJF, also over Antarctica.

Over the North American continent, Greenland and Eurasia, $\delta^{18}O_{precip}$ was depleted (Fig. 10b) in the summer (JJA) compared to PI along with a reduction in the surface temperature (not shown). In contrast, an enrichment of $\delta^{18}O_{precip}$ during summer was simulated over the tropics and monsoonal regions, where the precipitation was lower than in the control run.

### 6.2.3 Topography

In comparison with the control run, the $\delta^{18}O_{precip}$ in the DJF season (Fig. 9c) was depleted by 4‰ to 10‰, along with the uniform lowering of surface temperature over the ice-sheet topography, also over Eurasia and Antarctica by smaller magnitudes.

The JJA anomaly of $\delta^{18}O_{precip}$ from the PI control showed a corresponding depletion of 1‰ to 8‰ over the ice-sheets (Fig. 10c) with the lowering of surface temperature. $\delta^{18}O_{precip}$ was enriched over the Southern North American continent, which followed





CPD
8, 1319–1368, 2012



mostly a decrease in the amount of precipitation by 1 mm day$^{-1}$ to 3 mm day$^{-1}$ and the north-south gradient of surface temperature. The precipitation was also reduced in the summer months compared to the PI experiment over Eurasia. A general depletion was simulated over the tropical regions along with an increase in the precipitation amount.

#### 6.2.4 Orbital

During boreal winter, an enrichment in the $\delta^{18}O_{precip}$ concentration (0.5 ‰ to 2 ‰) was simulated mainly in the Northern Hemisphere, with an increase in surface temperature by 1 °C to 3 °C while more depleted values are simulated over the tropics in comparison with PI (Fig. 9d).

In the JJA season $\delta^{18}O_{precip}$ showed a depletion over the Northern Hemisphere in comparison with the PI. The $\delta^{18}O_{precip}$ was enriched over Antarctica and Central Africa by 2 ‰, with an increase in the amount of precipitation by 1mm day$^{-1}$ to 3 mm day$^{-1}$.

#### 6.2.5 SST

In line with the reduced surface temperature, more depleted values for $\delta^{18}O_{precip}$ were simulated over the Northern and Southern Hemisphere landmasses in the DJF season of the LGM-SST experiment in comparison with the control run (Fig. 9e).

The JJA difference of $\delta^{18}O_{precip}$ with respect to the control run (Fig. 10e) showed a depletion over northern latitudes, along with the reduced surface temperature (2 °C to 10 °C). The magnitude of the depletion, however, was small in comparison with the winter anomaly (Fig. 9e). The $\delta^{18}O_{precip}$ was more enriched over the Tibetan plateau, Arabia, and the SW monsoon regions in general.

#### 6.2.6 LGM-combined

Over the Northern and Southern high latitudes, the $\delta^{18}O_{precip}$ was in general more depleted in the LGM winter (DJF) compared to the control run (Fig. 9f) where the





CPD
8, 1319–1368, 2012



surface temperature and precipitation were also reduced compared to PI winter. The precipitation rate over Antarctica, most of Asia and north of Africa did not differ from that of PI (not shown), while $\delta^{18}O_{precip}$ was enriched by 2‰ over Central Africa in association with reduced precipitation.

The $\delta^{18}O_{precip}$ was more depleted in the LGM-combined JJA season globally expect for the North African land mass and the South West monsoon regions when compared to the control run (Fig. 10f). This could be related to the regional decrease of precipitation during the LGM summer monsoon. The $\delta^{18}O_{precip}$ was more depleted over the Laurentide ice sheets by 8‰ to 12‰ when compared to the control summer.

### 6.3 Isotopic content of the atmospheric water vapor

The isotopic content of precipitation depends on the isotopic content of the atmospheric water vapor, which in turn changes with the atmospheric circulation. In the present study, the topography and LGM-combined experiments produced the greatest changes in the atmospheric circulation and $\delta^{18}O$ content of the water vapor. Therefore, we only focus on these experiments in the remainder of this section.

The isotopic content of water vapor at the 500 hPa level showed wintertime depletion (Fig. 11) over the ice-sheet in the topography experiment compared to the control run. The 500 hPa geopotential height field showed a split in the flow due to the topography, in agreement with previous LGM modeling experiments (Otto-Bliesner et al., 2006a). A trough in the geopotential height field indicated enhanced storminess over Eurasia and North Atlantic in the winter season of the LGM-combined simulation (Fig. 11a), with a ridge over Western North America and a trough over the east of the continent. The westerlies over central and Northern Greenland strengthened in the winter, causing a depletion of $\delta^{18}O$ in the water vapor over Greenland. In contrast, an enrichment of $\delta^{18}O$ in water vapor was found over the North Pacific and over Eastern Eurasia where a more easterly wind was simulated with respect to the PI experiment. Another feature of the 500 hPa winter circulation was enhanced trans-polar winds from Eurasia to the north eastern part of the North American continent in the topography as well as





CPD
8, 1319–1368, 2012



the LGM experiments. The winter enrichment over the North Pacific in the topography experiment (Fig. 11b middle) was absent from the LGM-combined experiment (Fig. 11b bottom).

$\delta^{18}O$ was more enriched over Greenland, the North Atlantic and North-Western Eurasia in the summer season of the LGM-combined experiment when compared with the control run (Fig. 12b bottom). This feature was also seen in the topography experiment with an enhanced enrichment over Eurasia and over the Laurentide ice sheet, and moderate enrichment over Northern Pacific. The circulation from Eurasia and the North Atlantic to the Central and south of Greenland was enhanced, along with a strengthening of the circumpolar winds (Fig. 12b middle).

## 7 Discussion

The sequential procedure used for the analysis of the influence of the different LGM boundary conditions on the climate enables us to understand the dependence of the $\delta^{18}O_{precip}$ distribution on different climate factors.

### 7.1 Simulated climates

The maximum decrease in surface temperature was simulated north of 50° N in all of the experiments, which can be taken as an evidence of polar amplification as detailed in Masson-Delmotte et al. (2006).

Decreasing the GHG levels to LGM concentration was not sufficient to reproduce the cooling in the Southern Hemisphere as suggested by the coupled atmosphere-ocean studies carried out by Broccoli and Manabe (1987b). Our results diverge from their conclusions, because they argue that extended continental ice and reduced $CO_2$ concentrations account for 90 % of the LGM cooling, and that the $CO_2$ reduction is the major reason behind the cooling of the Southern Hemisphere. However, the lack of an active ocean component and hence the absence of the ocean-atmosphere feedback





CPD
8, 1319–1368, 2012



mechanisms explain the minimal effect of the reduction of GHG concentrations to LGM levels on the climate of the GHG experiment.

A change in the albedo alters the absorption and reflection of solar radiation. The albedo effect of the ice sheets is more prominent in the boreal summer months than in the winter months, with a strong reduction of summer surface temperature over the Laurentide and Eurasian ice sheets and a corresponding depletion of $\delta^{18}O_{precip}$. The surface temperature gradient between the ice sheets and the adjacent ice-free areas produced an increased summer precipitation over the southern part of North America, Western North Atlantic and Mexico as also noted by Manabe and Broccoli (1985).

In the topography experiment a localized reduction of surface temperature and more depleted values of $\delta^{18}O_{precip}$ were simulated in the drier climate over the elevated land surface. The effects of the ice sheet topography were mainly confined to the Northern Hemisphere high latitudes, as an inter-hemispheric heat transport via ocean currents is missing in the experiments. The resulting cooling is much smaller than that obtained by Hewitt and Mitchell (1997), who used an atmospheric general circulation model with a mixed layer ocean model. They found that the combined effect of the albedo and topography of the ice-sheets could lead to about two-thirds of the glacial cooling.

The global mean temperature change of the orbital experiment was found to be the smallest among all the simulations, which was expected as the orbital parameters for the present day and the LGM do not differ considerably.

The SST played a decisive factor for the surface temperature reduction in the tropics and consequently the $\delta^{18}O_{precip}$ distribution. The zonal distribution of $\delta^{18}O_{precip}$ in the SST experiment followed the pattern of the LGM-combined experiment in the Southern Hemisphere and up to 30° N. The global mean cooling brought about by the SST experiment accounted for 67 % of the total reduction in the LGM-combined experiment. Yet, the SST effect in the atmosphere-only simulations might be overestimated compared to coupled climate simulations where air-sea interaction is possible.

The precipitation decreased substantially in the LGM-combined simulation, particularly in the Intertropical Convergence Zone and the monsoon regions as seen in





CPD
8, 1319–1368, 2012



previous studies (Shin et al., 2003). The global mean cooling of 4.1 °C simulated in the LGM-combined experiment is in agreement with other climate models (Otto-Bliesner et al., 2006a; Jouzel et al., 1994).

The experiments showed that the SST and topography changes brought about considerable changes in the distribution of annual-mean surface temperature and $\delta^{18}O_{precip}$. The LGM-SST produced a global response, whereas the topography and ice-sheet albedo had more local effects on the climate hence the $\delta^{18}O_{precip}$ distribution.

### 7.2 Seasonal cycle of $\delta^{18}O_{precip}$

As Jouzel et al. (1987) noted for the present-day climate, the seasonal cycle of $\delta^{18}O_{precip}$ is divided at the 30° S latitude, where the zero contour was found in all the experiments (Figs. 7b and 8b). North of this latitude more positive values were simulated for the seasonal contrast. This could be explained by the $\delta^{18}O_{precip}$-precipitation relation that predicts an enrichment of $\delta^{18}O_{precip}$ during the dry season. It has been argued that this pattern reflects the atmospheric circulation and that the isotopic minima and maxima in the different seasons represent the positions of ITCZ and the subtropical highs (Feng et al., 2009). Another mechanism that contributes to the isotopic minimum at the ITCZ is the recycling of detrained water vapor from tropical convective cells, which further depletes the $\delta^{18}O_{precip}$ (Risi et al., 2008).

During the boreal winter season, a large-scale reduction of surface temperature along with a depletion of $\delta^{18}O_{precip}$ over the northern high latitudes was simulated in the LGM-combined experiment when compared to the control run. The LGM-combined and LGM-SST simulations yielded an isotopic enrichment in the South West (SW) Asian monsoon region in the JJA season in comparison with PI, which points to the tropical amount effect. Studies based on pollen in marine sediments (Van Campo, 1986) suggest an arid SW summer monsoon during the LGM, also the coastal upwelling in the Arabian Sea during LGM was found to be less intense (Prell et al., 1980; Prell and Curry, 1981). Similarly, studies based on climate models subject to LGM boundary





CPD
8, 1319–1368, 2012



conditions (with or without an ice-covered Tibetan Plateau) find that the tropical climate was probably much drier and the SW summer monsoon weaker during the LGM (Manabe and Broccoli, 1985; Kutzbach and Guetter, 1986; Rind, 1987; Lautenschlager and Santer, 1991) also at the same time the Intertropical Convergence Zone (ITCZ) likely shifted southward. The absence of seasonality in the precipitation rate over Antarctica found in our experiments was also reported in Werner et al. (2001). A similar lack of seasonality over Greenland is found in all the simulations and could mean that the distribution of $\delta^{18}O_{precip}$ over Greenland is influenced by the North Atlantic Ocean, which in our simulations also shows a lack of seasonality. In this line of evidence we note that the SST experiment brought about the largest change in the $\delta^{18}O_{precip}$ distribution over Greenland.

### 7.3 Relationship with climate variables

The $\delta^{18}O_{precip}$-surface temperature relationship simulated by the PI experiment over Greenland is found to have a slope that is slightly smaller by 0.06 ‰ $^{\circ}C^{-1}$ compared to that inferred from observations (Johnsen et al., 1989, $\delta^{18}O = 0.67T - 13.7$ ‰, $T$ in $^{\circ}C$) and results from the ECHAM3 atmosphere model (Werner et al., 2000) and the Community Atmosphere Model, version 2.0 (Lee et al., 2007). Our experiments produce changes in the relationship between $\delta^{18}O_{precip}$ and surface temperature, with a reduction of the slope by 0.09 ‰ $^{\circ}C^{-1}$ over Greenland in the LGM-combined experiment. The tropical amount effect was simulated in the model and the slope obtained for the control run was comparable in magnitude with the slope derived from the observed values at the tropical marine stations selected from the GNIP data base ($-0.55$ ‰ per mm day$^{-1}$, Bony et al., 2008; Cole et al., 1999). The changes in the $\delta^{18}O_{precip}$-precipitation relationship with the LGM boundary conditions are negligible, except for the SST and LGM-combined experiments. The inaccurate representation of $\delta^{18}O_{precip}$ in the model over Antarctica causes a reduced slope in the control run when compared to the observations (Masson-Delmotte et al., 2008). The inability of isotope models to accurately





CPD
8, 1319–1368, 2012



simulate the present-day distribution of isotopes over the southern polar regions, and the failure to reproduce the inland depletion was discussed in Werner et al. (2000) and Lee et al. (2007) and also thoroughly studied in Masson-Delmotte et al. (2008). The $\delta^{18}O_{precip}$-surface temperature relationship over Antarctica in the PI simulation deviates from the observations by Dahe et al. (1994), who derive a slope of 0.84 ‰ °C$^{-1}$, and by Masson-Delmotte et al. (2008), who obtained a slope of 0.80 ‰ °C$^{-1}$. Generally, the spatial slopes obtained for the control and LGM climates are similar, as in the results obtained by, for example, Jouzel et al. (1994).

### 7.4 Regional annual mean of $\delta^{18}O_{precip}$

The regional annual mean of $\delta^{18}O_{precip}$ over the North American ice sheets for the LGM-combined experiment is −24 ‰ (Table 5), which is less depleted compared to the −31 ‰ derived from ice core data for the Laurentide ice sheet (Duplessy et al., 2002). The maximum depletion over the Laurentide ice sheet was simulated in the LGM-combined experiment with a 10 ‰ difference from the control experiment. The topography change alone brought about a depletion of 3 ‰ over the ice-sheets, while albedo and SST changes brought down the $\delta^{18}O_{precip}$ by 1 ‰ each. The altitude effect (Dansgaard, 1964) in the topography experiment was evident from the difference to the ice-sheet albedo experiment.

The mean value of −17 ‰ in the LGM-combined experiment over Eurasia was comparatively enriched with respect to the range of −16 ‰ to −40 ‰ proposed by Duplessy et al. (2002). The annual-mean difference simulated between the LGM-combined and PI experiments over Greenland (Table 5) was smaller than the 4.7 ‰ difference in $\delta^{18}O_{precip}$ obtained from GISP2 (Johnsen et al., 2001) and also smaller than the $(-4.1 \pm 2.6)$ ‰ depletion simulated by the ECHAM isotopic model for the summit (Werner et al., 2001). The simulated annual-mean surface temperature over Central Greenland in the LGM-combined experiment was found to be higher than the





CPD
8, 1319–1368, 2012



reconstructed value (Cuffey and Clow, 1997). The over-estimation of surface temperature over Greenland in our model could explain the heavier $\delta^{18}O_{precip}$ value.

Over Southern South America, the annual-mean depletion was stronger in the SST and LGM-combined experiments compared to the control climate. Previous studies (Clapperton, 1993; Thompson et al., 2000) suggest a drier climate over South America during the LGM (25 % of land classified as desert), with colder tropical oceans and weaker inflow of moisture from the ocean. The response of the $\delta^{18}O_{precip}$ to the LGM-combined and LGM-SST forcing hints at the influence of the Atlantic Ocean, Pacific Ocean and Caribbean Sea, which are the major sources of moisture for this continent (Rozanski and Araguas., 1995). Sylvestre (2009) suggests prevailing drier conditions in Northern South America and the wetter southern part of the continent. The ITCZ and the wetter zones in Southern South America are expected to be the reason for the depleted values simulated in this region. The positive annual-mean $\delta^{18}O_{precip}$ anomalies simulated over North Africa, especially in the Sahel region in all the experiments in which a significant precipitation anomaly was absent could be attributed to the reduced precipitation and underestimation of surface temperature in the model in this arid region. Furthermore, it has been suggested that $\delta^{18}O_{precip}$ is related to large-scale regional precipitation rather than local precipitation (Schmidt et al., 2007; Tindall et al., 2009).

The simulated annual-mean anomaly of $\delta^{18}O_{precip}$ over Antarctica in the LGM-combined experiment agrees reasonably well with the observed difference from the present-day value of 3 ‰ to 5 ‰ in the Vostok ice core (Lorius et al., 1985).

### 7.5 Changes in the atmospheric circulation

It is suggested that the atmospheric circulation in the LGM was considerably different from the present-day configuration, owing to the elevated ice-sheet orography and increased sea-ice in high latitudes (Broccoli and Manabe, 1987a; Shin et al., 2003; Otto-Bliesner et al., 2006a). Distinct changes in the north polar circulation were





CPD
8, 1319–1368, 2012



indeed simulated in our topography and LGM-combined experiments with associated differences in the distribution of $\delta^{18}O$ in vapor.

Previous studies (Werner et al., 2001; Charles et al., 1994) identify the near-by polar seas, the North Atlantic and North Pacific Oceans and the North American and Eurasian continents as the source regions for glacial Greenland precipitation. When compared to modern conditions, the ice sheets caused a significant reduction of the contribution of moisture from the North American continent. Werner et al. (2001) also observe a southward shift of moisture transport from the North Atlantic and North America to Greenland. Kageyama and Valdes (2000) suggest that in Greenland, the winter precipitation during the LGM is lower because of the changes in atmospheric circulation and the southward deviation of the storm tracks due to the Laurentide ice-sheet, extended sea ice, and also because of the modified latitudinal SST gradient. In our simulation, this reduction in winter precipitation brought about an enrichment in the northern part of Greenland and near Nares Strait in the topographic and LGM-combined simulations as compared to the control simulation. The drier air mass advected over Greenland causes less precipitation during the winter season. The warmer and drier air mass over the ridge in the geopotential height field near the margin of the Laurentide ice sheets may have led to depleted $\delta^{18}O$ values during the winter in both the topography and LGM-combined simulations. The increased northerly flows and trans-polar advection of colder and drier air-masses at the 500 hPa level during the LGM would also have contributed to the drier conditions and more depleted values during the DJF season. The enrichment of heavy isotopes seen in the JJA season of LGM-combined and topography simulations over Greenland could be attributed to the advection of enriched water vapor from the North Atlantic and Eurasia, which agrees with Charles et al. (1994), while the North Pacific source of moisture in Northern Greenland was not evident in the results.





CPD
8, 1319–1368, 2012



## 8 Conclusions

The experiments that we conducted allow us to assess the effect of the individual climatic boundary conditions on the climate of the LGM one at a time, although a complete factor separation analysis (Stein and Alpert, 1993) was beyond the scope of this study.

Our simulations indicate that the changes in topography due to the large continental ice sheets and the changes in SST were the two predominant forcing factors for the climate of the LGM and hence the distribution of oxygen isotopes in precipitation, $\delta^{18}O_{precip}$. The altitude effect and the changes in atmospheric circulation brought about by the LGM topography led to a depletion of $\delta^{18}O_{precip}$ in the high latitudes of the Northern Hemisphere. The temperature and $\delta^{18}O_{precip}$ show a linear relationship in this region, and the slopes for the LGM and PI climates are similar. Overall, the albedo and topography of the ice-sheets have a local effect on the surface temperature and precipitation, and the distribution of $\delta^{18}O_{precip}$ appears to be influenced by these local changes in surface temperature.

The simulated relationship between the $\delta^{18}O_{precip}$ and climate variables is found to be rather insensitive to changes from PI to full LGM boundary conditions. A strong seasonality is lacking in the surface distribution of $\delta^{18}O_{precip}$ over Greenland in all the simulations, which points to an oceanic source of moisture. In contrast, an isotopic seasonality related to the precipitation amount effect is found over the tropical monsoon regions in our LGM-combined and SST simulations, where the colder and drier Asian continent during the LGM caused a reduction of the land-sea temperature gradient and hence the intensity of the SW monsoon.

*Acknowledgements.* This project was funded by the DFG (Deutsche Forschungsgemeinschaft) within the European Graduate College "Proxies in Earth History."





CPD
8, 1319–1368, 2012



## References


Berger, A.: Long-term variations of daily insolation and Quaternary climatic changes, J. Atmos. Sci., 35(12), 2362–2367, 1978.

Bonan, G. B., Oleson, K. W., Vertenstein, M., Levis, S., Zeng, X., Dai, Y., Dickinson, R. E., and Yang, Z.-L.: The land surface climatology of the Community Land Model coupled to the NCAR Community Climate Model, J. Climate, 15, 3123–3149, 2002.

Bony, S., Risi, C., and Vimeux, F.: Influence of convective processes on the isotopic composition ($\delta$O18 and $\delta$D) of precipitation and water vapor in the tropics: 1. Radiative-convective equilibrium and TOGA-COARE simulations, J. Geophys. Res., 113, D19305, doi:10.1029/2008JD009942, 2008.

Broccoli, A. J. and Manabe, S.: The effects of the Laurentide ice sheet on north american climate during the last glacial maximum, Geogr. Phys. Quatern., 41, 291–299, 1987a.

Broccoli, A. J. and Manabe, S.: The influence of continental ice, atmospheric $CO_2$, and land albedo on the climate of the last glacial maximum, Clim. Dynam., 1, 87–99, 1987b.

Braconnot, P., Otto-Bliesner, B., Harrison, S., Joussaume, S., Peterchmitt, J.-Y., Abe-Ouchi, A., Crucifix, M., Driesschaert, E., Fichefet, Th., Hewitt, C. D., Kageyama, M., Kitoh, A., Laîné, A., Loutre, M.-F., Marti, O., Merkel, U., Ramstein, G., Valdes, P., Weber, S. L., Yu, Y., and Zhao, Y.: Results of PMIP2 coupled simulations of the Mid-Holocene and Last Glacial Maximum – Part 1: experiments and large-scale features, Clim. Past, 3, 261–277, doi:10.5194/cp-3-261-2007, 2007.

Charles, C. D., Rind, D., Jouzel, J., Koster, R. D., and Fairbanks, R. G.: Glacial-interglacial changes in moisture sources for Greenland: influences on the ice core record of climate, Science, 263, 508–511, 1994.

Clapperton, C. M.: Nature of environmental changes in South America at the Last Glacial Maximum, Palaeogeogr. Palaeocl., 101, 189–208, 1993.

Cole, J. E., Rind, D., Webb, R. S., Jouzel, J., and Healy, T.: Climatic controls on interannual variability of precipitation $\delta^{18}$O: the simulated influence of temperature, precipitation amount, and vapour source region, J. Geophys. Res., 104, 14223–14235, 1999.

Collins, W. D., Rasch, P. J., Boville, B. A., Hack, J. J., McCaa, J. R., Williamson, D. L., and Briegleb, B.: The formulation and atmospheric simulation of the Community Atmospheric Model version 3 (CAM3), J. Climate, 19, 2144–2161, 2006.






CPD
8, 1319–1368, 2012



Craig, H. and Gordon, L. I.: Deuterium and oxygen 18 variations in the ocean and marine atmosphere, in: Proc. Stable Isotopes in Oceanographic Studies and Paleotemperatures, Cons. Naz. Ric. Lab. Geol. Nucl., Pisa, 9–130, 1965.
Cuffey, K. M. and Clow, G. D.: Temperature, accumulation, and ice sheet elevation in Central Greenland through the last deglacial transition, J. Geophys. Res., 102, 26383–26396, 1997.
Dahe, Q., Petit, J. R., Jouzel, J., and Stievenard, M.: Distribution of stable isotopes in surface snow along the route of the 1990 International Trans-Antarctica Expedition, J. Glaciol., 40, 107–118, 1994.
Dahl-Jensen, D., Mosegaard, K., Gundestrup, N., Clow, G. D., Johnsen, S., Hansen, A. W., and Balling, N.: Past temperature directly from the Greenland Ice Sheet, Science, 282, 268–271, 1998.
Dansgaard, W.: Stable isotopes in precipitation, Tellus, 16, 436–68, 1964.
Dansgaard, W., Johnsen, S. J., Clausen, H. B., and Gundestrup, N.: Stable isotope glaciology, Medd. Grønland, 197, 1–53, 1973.
Deardoff, J. W.: A parameterization of moisture content for use in atmospheric prediction model, J. Appl. Meteorol., 16, 1182–1185, 1977.
Dickinson, R. E., Oleson, K. W., Bonan, G., Hoffman, F., Thornton, P., Vertenstein, M.,Yang, Z.-L., and Zeng, X.: The Community Land Model and its climate statistics as a component of the Community Climate System Model, J. Climate, 19, 2302–2324, 2006.
Duplessy, J. C., Labeyrie, L. D., and Waelbroeck, C.: Constraints on the ocean oxygen isotopic enrichment between the last glacial maximum and the Holocene: paleoceanographic implications, Quaternary Sci. Rev., 21(1–3), 315–330, doi:10.1016/S0277-3791(01)00107-X, 2002.
Fairbanks, R. G.: A 17000-year glacio-eustatic sea level record: influence of glacial melting rates on the Younger Dryas event and deep-ocean circulation, Nature, 342, 637–642, 1989.
Feng, X., Faiia, A. M., and Posmentier, E. S.: Seasonality of isotopes in precipitation: a global perspective, J. Geophys. Res., 114, D08116, doi:10.1029/2008JD011279, 2009.
Hack, J. J., Caron, J. M., Yeager, S. G., Oleson, K. W., Holland, M. M., Truesdale, J. E., and Rasch, P. J.: Simulation of the global hydrological cycle in the CCSM Community Atmosphere Model Version 3 (CAM3): mean features, J. Climate, 19(11), 2199–2221, 2006.
Hewitt, C. D. and Mitchell, J. F. B.: Radiative forcing and response of a GCM to ice age boundary conditions: cloud feedback and climate sensitivity, Clim. Dynam., 13, 821–834, 1997.





CPD
8, 1319–1368, 2012



Hoffmann, G., Werner, M., and Heimann, M.: Water isotope module of the ECHAM atmospheric general circulation model: A study on timescales from days to several years, J. Geophys. Res., 103(D14), 16871–16896, 1998.

IAEA/WMO.: Global Network of Isotopes in Precipitation: The GNIP database, available at: http://www-naweb.iaea.org/napc/ih/IHS_resources_gnip.html (last access: 10 January 2012), 2006.

Johnsen, S. J., Dansgaard, W., and White, J. W. C.: The origin of Arctic precipitation under present and glacial conditions, Tellus B, 41, 452–468, 1989.

Johnsen, S. J., Dahl-Jensen, D., Gundestrup, N., Steffensen, J. P., Clausen, H. B., Miller, H., Masson-Delmotte, V., Sveinbjörnsdottir, A. E., and White, J.: Oxygen isotope and palaeotemperature records from six Greenland ice-core stations: Camp Century, Dye-3, GRIP, GISP2, Renland and NorthGRIP, J. Quaternary Sci., 16, 299–308, 2001.

Jouzel, J., Koster, R. D., Suozzo, R. J., Russel, G. L., White, J. W. C., and Broecker, W. S.: Simulations of the HDO and H218O atmospheric cycles using the NASA GISS general circulation model: the seasonal cycle for present-day conditions, J. Geophys. Res., 92(D12), 14739–14760, 1987.

Jouzel, J., Koster, R. D., Suozzo, R. J., and Russell, G. L.: Stable water isotope behavior during the last glacial maximum: a general circulation model analysis, J. Geophys. Res., 99, 25791–25801, 1994.

Kageyama, M. and Valdes, P.: Impact of the North American ice-sheet orography on the Last Glacial Maximum eddies and snowfall, Geophys. Res. Lett., 27(10), 1515–1518, 2000.

Kutzbach, J. E. and Guetter, P. J.: The influence of changing orbital parameters and surface boundary conditions on climate simulations for the past 18 000 years, J. Atmos. Sci., 43, 1726–1759, 1986.

Lambeck, K. and Chappell, J.: Sea level change through the last glacial cycle, Science, 292, 679–686, 2001.

Lautenschlager, M. and Santer, B. D.: Atmospheric response to a hypothetical Tibetan Ice Sheet, J. Climate, 4, 386–394, 1991.

Lee, J. E., Fung, I., DePaolo, D. J., and Henning, C. C.: Analysis of the global distribution of water isotopes using the NCAR atmospheric general circulation model, J. Geophys. Res., 112, D16306, doi:10.1029/2006JD007657, 2007.





CPD
8, 1319–1368, 2012



Lee, J. E., Fung, I., DePaolo, D. J., and Otto-Bliesner, B. L.: Water isotopes during the Last Glacial Maximum: new GCM calculations, J. Geophys. Res., 113, D19109, doi:10.1029/2008JD009859, 2008.

Lorius, C., Jouzel, J., Ritz, C., Merlivat, L., Barkov, N. I., Korotkevich, Y. S., and Kotlyakov, V. M.: A 150 000-year climatic record from Antarctic ice, Nature, 316, 591–596, 1985.

Manabe, S.: Climate and the ocean circulation: 1. The atmospheric circulation and the hydrology of the earth's surface, Mon. Weather Rev., 97, 739–805, 1969.

Manabe, S. and Broccoli, A. J.: The influence of continental ice sheets on the climate of an ice age, J. Geophys. Res., 90, 2167–2190, 1985.

Masson-Delmotte, V., Kageyama, M., Braconnot, P., Charbit, S., Krinner, G., Ritz, C., Guilyardi, E., Jouzel, J., Abe-Ouchi, A., Crucifix, M., Gladstone, R. M., Hewitt, C. D., Kitoh, A., Legrande, A., Marti, O., Merkel, U., Motoi, T., Ohgaito, R., Otto-Bliesner, B., Peltier, W. R., Ross, I., Valdes, P. J., Vettoretti, G., Weber, S. L., and Wolk, F.: Past and future polar amplification of climate change: climate model intercomparisons and ice-core constraints, Clim. Dynam., 26, 513–529, 2006.

Masson-Delmotte, V., Hou, S., Ekaykin, A., Jouzel, J., Aristarain, A., Bernardo, R. T., Bromwhich, D., Cattani, O., Delmotte, M., Falourd, S., Frezzotti, M., Gallée, H., Genoni, L., Isaksson, E., Landais, A., Helsen, M., Hoffmann, G., Lopez, J., Morgan, V., Motoyama, H., Noone, D., Oerter, H., Petit, J. R., Royer, A., Uemura, R., Schmidt, G. A., Schlosser, E., Simões, J. C., Steig, E., Stenni, B., Stievenard, M., van den Broeke, M., Van de Wal, R., Van den Berg, W.-J., Vimeux, F., and White, J. W. C.: A review of Antarctic surface snow isotopic composition: observations, atmospheric circulation and isotopic modelling, J. Climate, 21, 3359–3387, 2008.

Merkel, U., Prange, M., and Schulz, M.: ENSO variability and teleconnections during glacial climate, Quaternary Sci. Rev., 29, 86–100, 2010.

Noone, D.: Water isotopes in CCSM for studying water cycles in the climate system, paper presented at CCSM Sci. Steering Comm., 8th Annual CCSM Workshop, Breckenridge, Colorado, June, 2003.

Noone, D.: Isotopic composition of water vapor modeled by constraining global climate simulations with reanalyses, in: Research Activities in Atmospheric and Oceanic Modeling, edited by: Cote, J., Report No. 35, World Meteorological Organization, 2–37, 2006.

Noone, D. and Simmonds, I.: Associations between d18O of water and climate parameters in a simulation of atmospheric circulation for 1979–95, J. Climate, 15(22), 3150–3169, 2002.





CPD
8, 1319–1368, 2012



Noone, D. and Sturm, C.: Comprehensive dynamical models of global and regional water isotope distributions, in: Isoscapes: Understanding Movement, Pattern, and Process on Earth through Isotope Mapping, Springer Verlag, Dordrecht, 2009.
Otto-Bliesner, B. L., Brady, E. C., Clauzet, G., Tomas, R., Levis, S., and Kothavala, Z.: Last glacial maximum and Holocene climate in CCSM3, J. Climate, 19, 2526–2544, 2006a.
Otto-Bliesner, B. L., Tomas, R., Brady, E. C., Ammann, C., Kothavala, Z., and Clauzet, G.: Climate sensitivity of moderate- and low-resolution versions of CCSM3 to pre-industrial forcings, J. Climate, 19, 2567–2583, 2006b.
Peltier, W. R.: Global glacial isostasy and the surface of the ice-age Earth: the ICE-5G (VM2) model and GRACE, Annu. Rev. Earth Planet. Sci., 32, 111–149, 2004.
Petit, J. R., Jouzel, J., Raynaud, D., Barkov, N. I., Barnola, J.-M., Basile, I., Bender, M., Chappellaz, J., Davis, M., Delaygue, G., Delmotte, M., Kotlyakov, V. M., Legrand, M., Lipenkov, V. Y., Lorius, C., Pe'pin, L., Ritz, C., Saltzman, E., and Stievenard.: Climate and atmospheric history of the past 420 000 years from the Vostok ice core, Antarctica, Nature, 399, 429–436, 1999.
Prell, W. L. and Curry, W. B.: Faunal and isotopic indices of monsoonal upwelling: Western Arabian Sea, Oceanol. Acta, 4, 91–98, 1981.
Prell, W. L., Hutson, W. H., Williams, D. F., Be, A. W. H., Geitzenauer, K., and Molfino, B.: Surface circulation of the Indian Ocean during the Last Glacial Maximum, approximately 18 000 yr BP, Quaternary Res., 14, 309–336, 1980.
Rind, D.: Components of the ice age circulation, J. Geophys. Res., 92, 4241–4281, 1987.
Risi, C., Bony, S., and Vimeux, F.: Influence of convective processes on the isotopic composition (d18O and dD) of precipitation and water vapor in the tropics: 2. Physical interpretation of the amount effect, J. Geophys. Res., 113, D19306, doi:10.1029/2008JD009943, 2008.
Rozanski, K. and Araguas-Araguas, L.: Spatial and temporal variability of stable isotope composition of precipitation over the South American Continent, Bull. Inst. Fr. Etudes Andines., 24, 379–390, 1995.
Rozanski, K., Araguas-Araguas, L., and Gonfiantini, R.: Isotopic patterns in modern global precipitation, In: Climate Change in Continental Isotopic Records, 1–36, Geophys. Monograph, 78, 1993.
Schmidt, G. A., LeGrande, A. N., and Hoffmann, G.: Water isotope expressions of intrinsic and forced variability in a coupled ocean-atmosphere model, J. Geophys. Res., 112, D10103, doi:10.1029/2006JD007781, 2007.





CPD
8, 1319–1368, 2012



Shin, S. I., Liu, Z., Otto-Bliesner, B. L., Brady, E. C., Kutzbach, J. E., and Harrison, S. P.: A simulation of the Last Glacial Maximum climate using the NCAR CSM, Clim. Dynam., 20, 127–151, 2003.

Stein, U. and Alpert, P.: Factor separation in numerical simulations, J. Atmos. Sci., 50, 2107–2115, 1993.

Stenni, B., Masson-Delmotte, V., Johnsen, S., Jouzel, J., Longinelli, A., Monnin, E., Rothlisberger, R., and Selmo, E.: An oceanic cold reversal during the last deglaciation, Science, 293, 2074–2077, 2001.

Sturm, C., Zhang, Q., and Noone, D.: An introduction to stable water isotopes in climate models: benefits of forward proxy modelling for paleoclimatology, Clim. Past, 6, 115–129, doi:10.5194/cp-6-115-2010, 2010.

Sylvestre, F.: Moisture pattern during the last Glacial Maximum in South America, in: Past Climate Variability in South America and Surrounding Regions, Springer Netherlands, 2009.

Thompson, L. G., Mosley-Thompson, E., and Henderson, K. A.: Ice-core palaeoclimate records in tropical South America since the Last Glacial Maximum, J. Quaternary Sci., 15, 377–394, 2000.

Tindall, J. C., Valdes, P., and Sime, L. C.: Stable water isotopes in HadCM3: Isotopic signature of El Niño–Southern Oscillation and the tropical amount effect, J. Geophys. Res., 114, D04111, doi:10.1029/2008JD010825, 2009.

Van Campo, E.: Monsoon fluctuations in two 20,000-yr B.P. oxygen-isotope/pollen records off South-west India, Quaternary Res., 26, 376–388, 1986.

Werner, M., Mikolajewicz, U., Heimann, M., and Hoffmann, G.: Borehole versus isotope temperatures on Greenland: Seasonality does matter, Geophys. Res. Lett., 27, 723–726, 2000.

Werner, M., Heimann, M., and Hoffmann, G.: Isotopic composition and origin of polar precipitation in present and glacial climate simulations, Tellus B, 53, 53–71, 2001.

Williamson, D. L. and Olson, J. G.: Climate simulations with a Semi-Lagrangian version of the NCAR community climate model, Mon. Weather Rev., 122, 1594–1610, 1994.

Williamson, D. L. and Rasch, P. J.: Water vapor transport in the NCAR CCM2, Tellus A, 46, 34–51, 1993.





CPD
8, 1319–1368, 2012



**Table 1.** Summary of experiments and boundary conditions.

| Experiment | SST | Orbital year | Topography | GHG | Glacier |
|---|---|---|---|---|---|
| PI | PI | 1950 | PI[1] | PI | PI[2] |
| $GHG_{(LGM)}$ | PI | 1950 | PI | LGM | PI |
| $Albedo_{(LGM)}$ | PI | 1950 | PI | PI | LGM |
| $Topography_{(LGM)}$ | PI | 1950 | LGM | PI | PI |
| $SST_{(LGM)}$ | LGM | 1950 | PI | PI | PI |
| $Orbital_{(LGM)}$ | PI | 21 ka | PI | PI | PI |
| LGM-combined | LGM | 21 ka | LGM | LGM | LGM |

[1,2] Present day values are used for the ice-sheet topography and coast lines in the PI (control) simulation following the PMIP2 protocol.





CPD
8, 1319–1368, 2012



**Table 2.** Atmospheric greenhouse gas concentrations for the PI and LGM time periods.

| Greenhouse gases | Pre-industrial | LGM |
|---|---|---|
| $CO_2$ (ppmv) | 280 | 185 |
| $CH_4$ (ppbv) | 760 | 350 |
| $N_2O$ (ppbv) | 270 | 200 |





CPD
8, 1319–1368, 2012



**Table 3.** Annual mean surface temperature (TS) in ˚C over the globe ($TS_{global}$), land points alone ($TS_{land}$), Northern and Southern Hemispheres ($TS_{NH}$, $TS_{SH}$), and tropics ($TS_{tropics}$; 20˚ S to 20˚ N) in the different experiments. The difference to the control experiment is given in the adjacent columns.

| Experiment | $TS_{global}$ | | $TS_{land}$ | | $TS_{NH}$ | | $TS_{SH}$ | | $TS_{tropics}$ | |
|---|---|---|---|---|---|---|---|---|---|---|
| PI | 12.89 | | 6.70 | | 13.057 | | 13.01 | | 25.66 | |
| $GHG_{(LGM)}$ | 12.75 | –0.14 | 6.28 | –0.42 | 12.82 | –0.24 | 12.96 | –0.05 | 25.63 | –0.03 |
| $Albedo_{(LGM)}$ | 12.71 | –0.18 | 6.08 | –0.62 | 12.69 | –0.37 | 13.00 | –0.01 | 25.66 | 0.00 |
| $Topography_{(LGM)}$ | 12.45 | –0.44 | 5.32 | –1.38 | 12.47 | –0.59 | 12.73 | –0.27 | 25.53 | –0.13 |
| $Orbital_{(LGM)}$ | 12.86 | –0.02 | 6.31 | –0.38 | 13.00 | –0.05 | 13.01 | 0.0 | 25.67 | 0.01 |
| $SST_{(LGM)}$ | 10.10 | –2.79 | 2.93 | –3.76 | 10.27 | –2.78 | 9.92 | –3.08 | 24.00 | –1.65 |
| LGM-combined | 8.79 | –4.1 | –0.52 | –7.22 | 8.35 | –4.71 | 9.58 | –3.42 | 23.84 | –1.83 |





CPD
8, 1319–1368, 2012



**Table 4.** Annual mean precipitation in mm day$^{-1}$ over the globe ($TS_{global}$), land points alone ($TS_{land}$), Northern and Southern Hemispheres ($TS_{NH}$, $TS_{SH}$), and tropics ($TS_{tropics}$; 20° S to 20° N) in the different experiments. The difference to the control experiment is given in adjacent columns.

| Experiment | $precip_{global}$ | | $precip_{land}$ | | $precip_{NH}$ | | $precip_{SH}$ | | $precip_{tropics}$ | |
|---|---|---|---|---|---|---|---|---|---|---|
| PI | 2.77 | | 2.10 | | 2.64 | | 2.90 | | 4.44 | |
| $GHG_{(LGM)}$ | 2.80 | 0.03 | 2.05 | –0.04 | 2.67 | 0.03 | 2.94 | 0.03 | 4.49 | 0.04 |
| $Albedo_{(LGM)}$ | 2.76 | –0.00 | 2.06 | –0.04 | 2.62 | –0.01 | 2.91 | 0.01 | 4.43 | –0.01 |
| $Topography_{(LGM)}$ | 2.75 | –0.01 | 2.12 | 0.01 | 2.61 | –0.02 | 2.89 | –0.01 | 4.40 | –0.04 |
| $Orbital_{(LGM)}$ | 2.77 | 0.0 | 2.10 | 0.0 | 2.64 | 0.0 | 2.90 | 0.0 | 4.43 | –0.01 |
| $SST_{(LGM)}$ | 2.55 | –0.22 | 1.98 | –0.12 | 2.39 | –0.24 | 2.70 | –0.20 | 4.15 | –0.28 |
| LGM-combined | 2.55 | –0.22 | 1.86 | –0.24 | 2.38 | –0.25 | 2.71 | –0.18 | 4.17 | –0.27 |





CPD
8, 1319–1368, 2012



**Table 5.** Annual mean $\delta^{18}O_{precip}$ (‰) as area averages for selected geographical regions in the different experiments. The difference to the control experiment is given in brackets below the numbers.

| Experiment | Laurentide Ice Sheets | Eurasian Ice Sheet | Greenland | N. Africa | S. Africa | N. South America | S. South America | Antarctica |
|---|---|---|---|---|---|---|---|---|
| PI | –13.84 | –12.02 | –20.12 | –3.90 | –6.38 | –4.96 | –5.01 | –28.28 |
| $GHG_{(LGM)}$ | –14.08 | –12.37 | –20.23 | –2.84 | –6.48 | –5.18 | –5.40 | –28.28 |
| | (–0.24) | (–0.35) | (–0.11) | (+1.06) | (–0.09) | (–0.21) | (–0.38) | (0.00) |
| $Albedo_{(LGM)}$ | –14.96 | –12.14 | –20.19 | –2.94 | –6.44 | –5.00 | –5.16 | –28.32 |
| | (–1.11) | (–0.12) | (–0.07) | (+0.96) | (–0.05) | (–0.03) | (–0.14) | (–0.04) |
| $Topography_{(LGM)}$ | –17.17 | –14.13 | –20.53 | –3.67 | –6.66 | –5.09 | –5.36 | –29.49 |
| | (–3.33) | (–2.11) | (–0.41) | (+0.22) | (–0.28) | (–0.12) | (–0.34) | (–1.21) |
| $Orbital_{(LGM)}$ | –14.01 | –12.16 | –20.05 | –2.54 | –6.59 | –5.05 | –5.31 | –28.27 |
| | (–0.16) | (–0.14) | (+0.06) | (+1.35) | (–0.21) | (–0.09) | (–0.29) | (+0.01) |
| $SST_{(LGM)}$ | –15.34 | –14.79 | –22.72 | –2.99 | –7.28 | –5.53 | –6.19 | –29.52 |
| | (–1.50) | (–2.77) | (–2.6) | (+0.91) | (–0.89) | (–0.57) | (–1.17) | (–1.24) |
| LGM-combined | –24.22 | –17.95 | –22.33 | –2.32 | –7.24 | –5.58 | –6.731 | –30.56 |
| | (–10.38) | (–5.93) | (–2.21) | (+1.57) | (–0.86) | (–0.62) | (–1.71) | (–2.27) |





CPD
8, 1319–1368, 2012



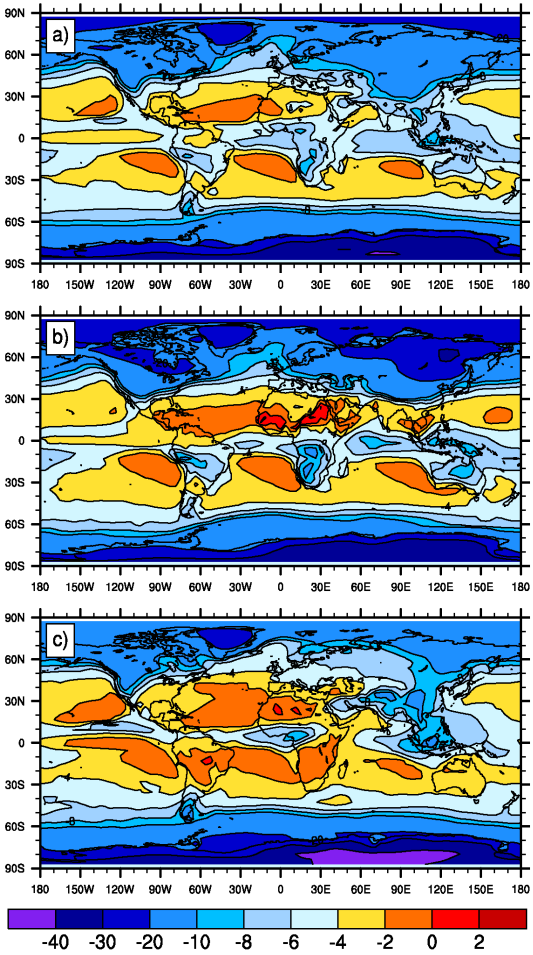


**Fig. 1.** Global distribution of $\delta^{18}O_{precip}$ (‰) for the control run: **(a)** annual mean, **(b)** December-January-February (DJF) season, **(c)** June-July-August (JJA) season.





CPD
8, 1319–1368, 2012



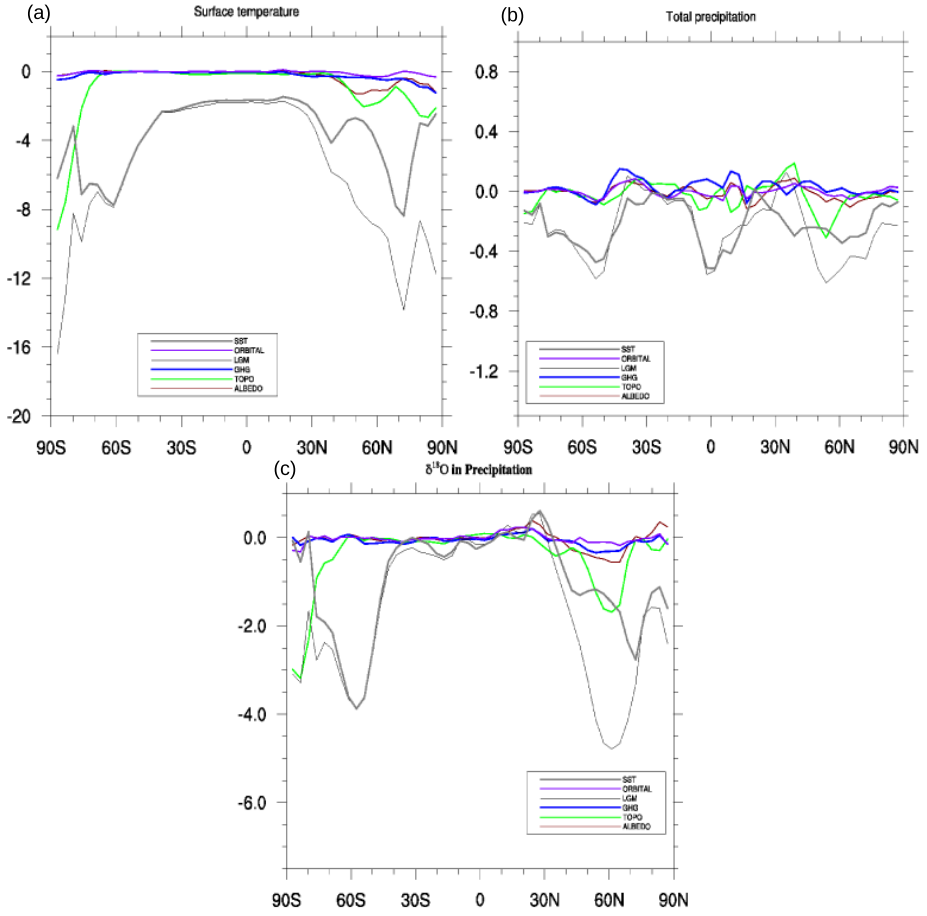


**Fig. 2.** The difference of zonal means of **(a)** surface temperature (°C), **(b)** total precipitation (mm day$^{-1}$), **(c)** $\delta^{18}O_{precip}$ (‰) of each experiment from the control run.





CPD
8, 1319–1368, 2012



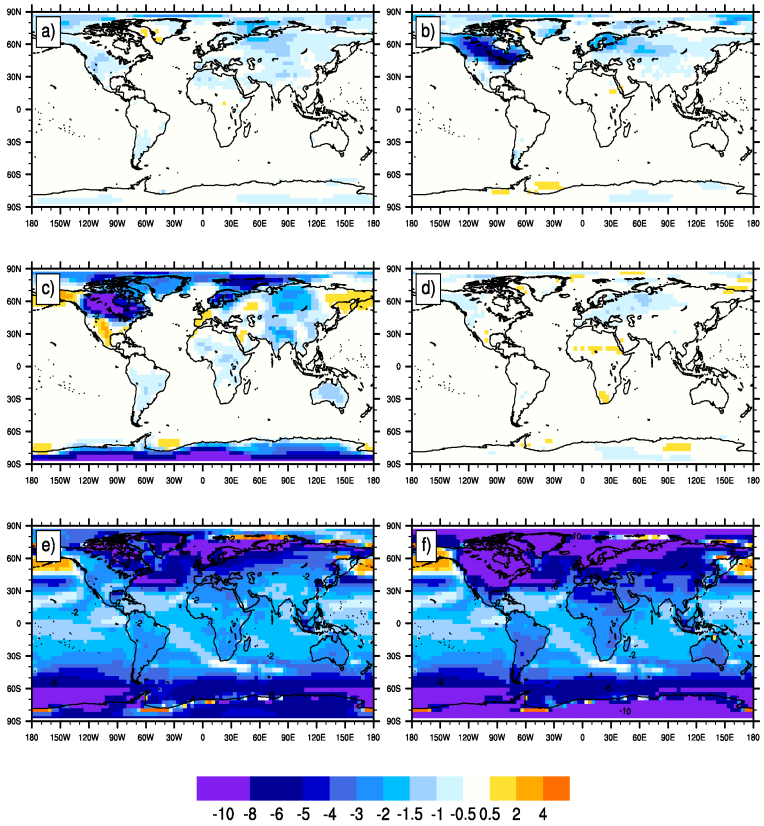


**Fig. 3.** Annual mean difference of surface temperature (°C) of **(a)** GHG, **(b)** albedo, **(c)** topography, **(d)** orbital, **(e)** SST, **(f)** LGM-combined experiments from the control run.





CPD
8, 1319–1368, 2012





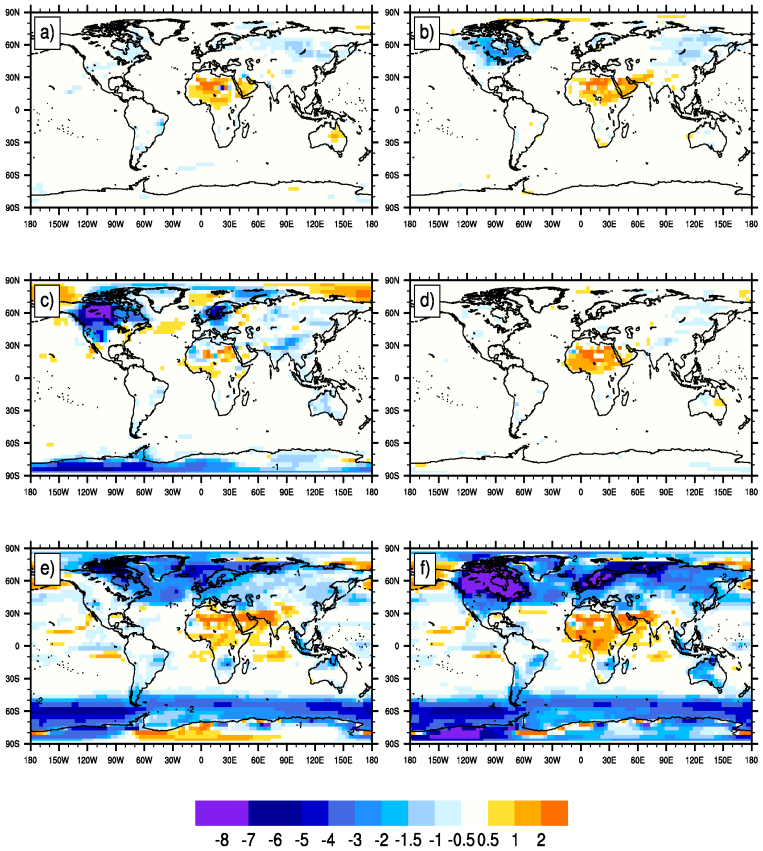


**Fig. 4.** Annual mean difference of $\delta^{18}O_{precip}$ (‰) of **(a)** GHG, **(b)** albedo, **(c)** topography, **(d)** orbital, **(e)** SST, **(f)** LGM-combined experiments from the control run.





CPD
8, 1319–1368, 2012





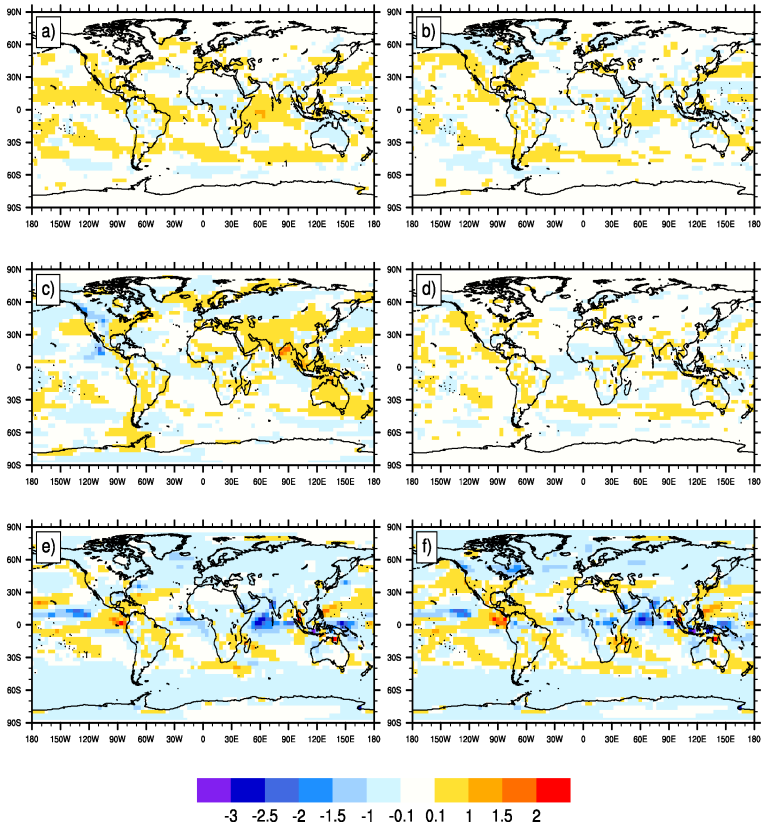


**Fig. 5.** Annual mean difference of total precipitation (mm day$^{-1}$) of **(a)** GHG, **(b)** albedo, **(c)** topography, **(d)** orbital, **(e)** SST, **(f)** LGM-combined experiments from the control run.





CPD
8, 1319–1368, 2012



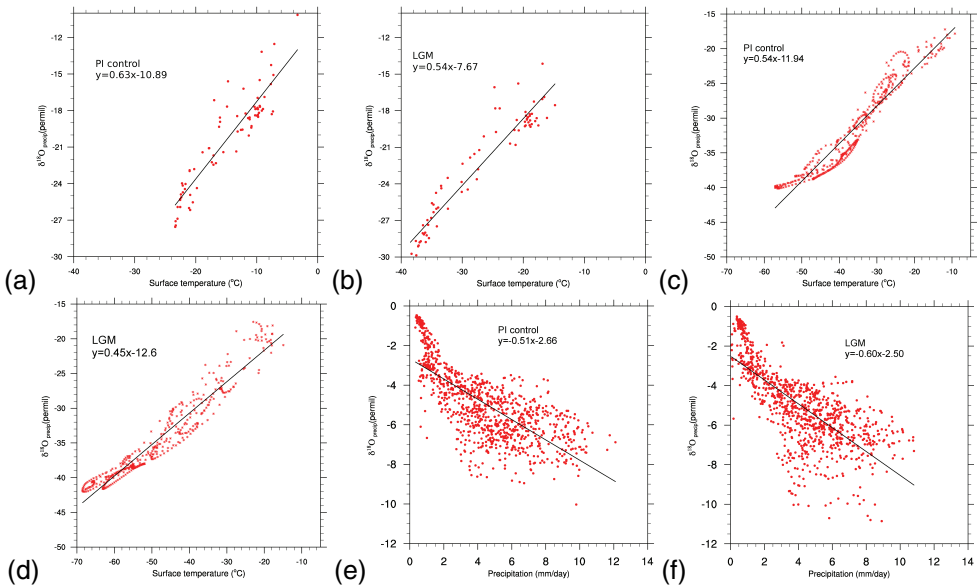


**Fig. 6.** The relationship between $\delta^{18}O_{precip}$ (‰) and surface temperature (°C) is shown for Greenland [**(a)** and **(b)**, where **(a)** PI control, **(b)** LGM-combined] and Antarctica [**(c)** and **(d)**, where **(c)** PI control, **(d)** LGM-combined]. The relationship between $\delta^{18}O_{precip}$ (‰) and precipitation (mm day$^{-1}$) is shown for the tropics [**(e)** and **(f)**, where **(e)** PI control, **(f)** LGM-combined].





CPD
8, 1319–1368, 2012



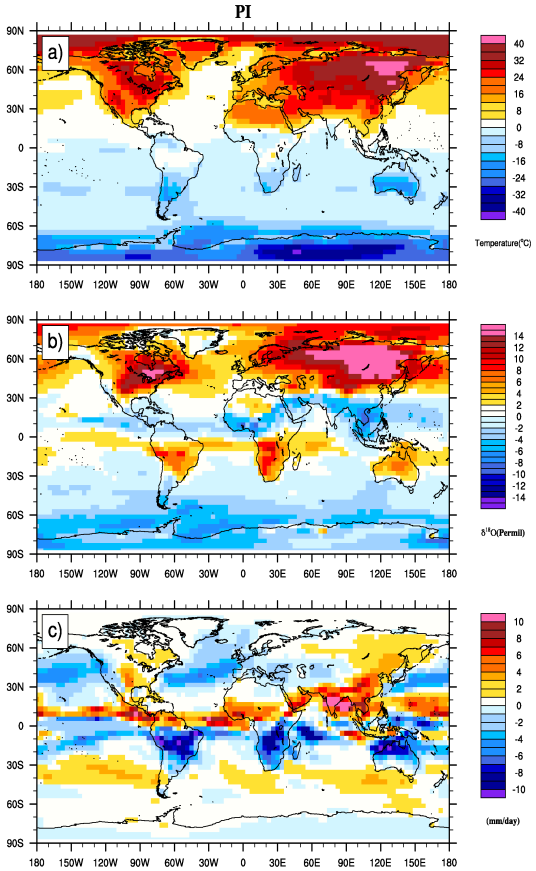


**Fig. 7.** The JJA–DJF difference of **(a)** surface temperature (°C), **(b)** $\delta^{18}O_{precip}$ (‰), **(c)** total precipitation (mm day$^{-1}$) of the control experiment.





CPD
8, 1319–1368, 2012



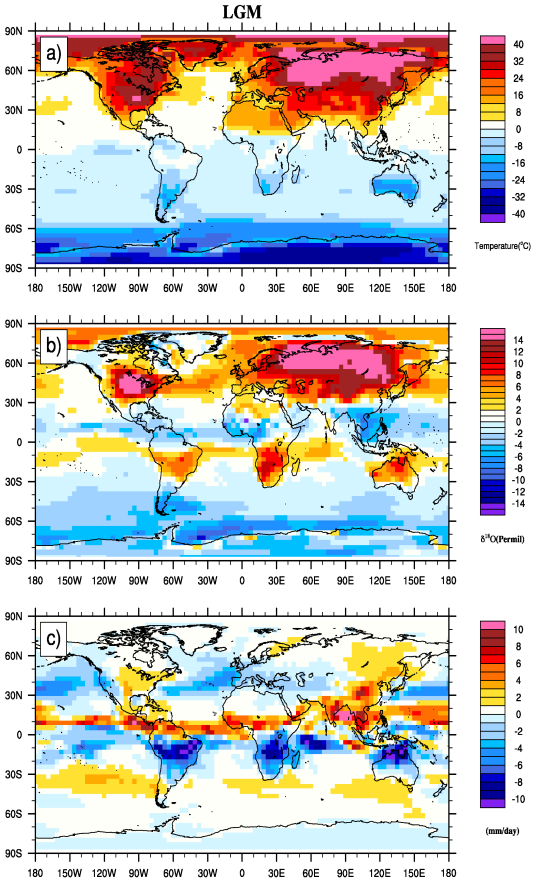


**Fig. 8.** The JJA-DJF difference of **(a)** surface temperature (°C), **(b)** $\delta^{18}O_{precip}$ (‰), total precipitation (mm day$^{-1}$) of the LGM-combined experiment.





CPD
8, 1319–1368, 2012



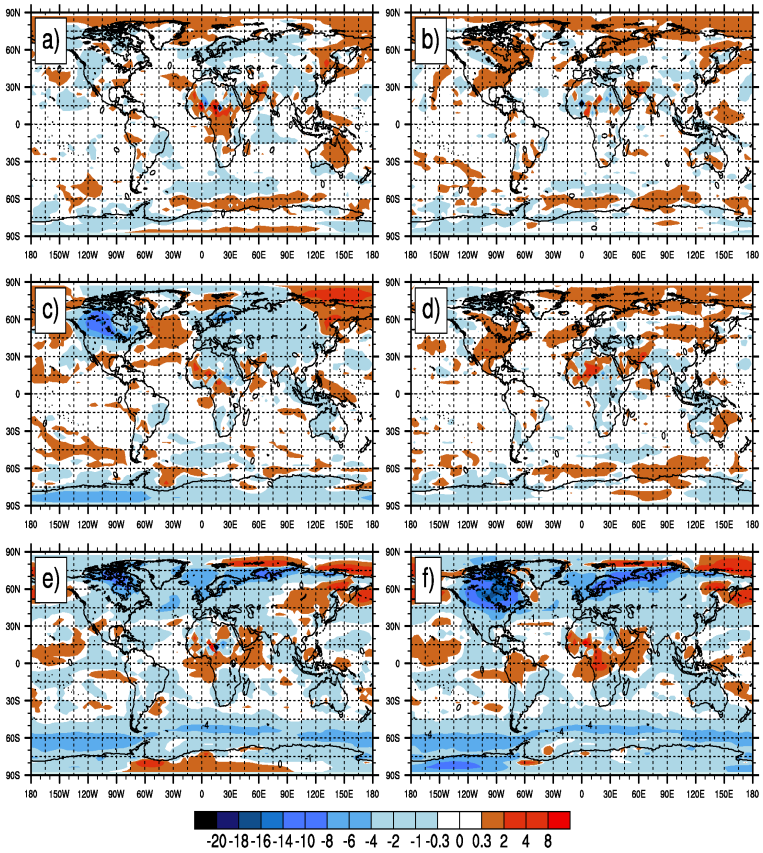


**Fig. 9.** The anomalies of $\delta^{18}O_{precip}$ (‰) for **(a)** GHG, **(b)** albedo, **(c)** topography, **(d)** orbital, **(e)** SST, **(f)** LGM-combined experiments from the control experiment for the boreal winter (DJF).





CPD
8, 1319–1368, 2012



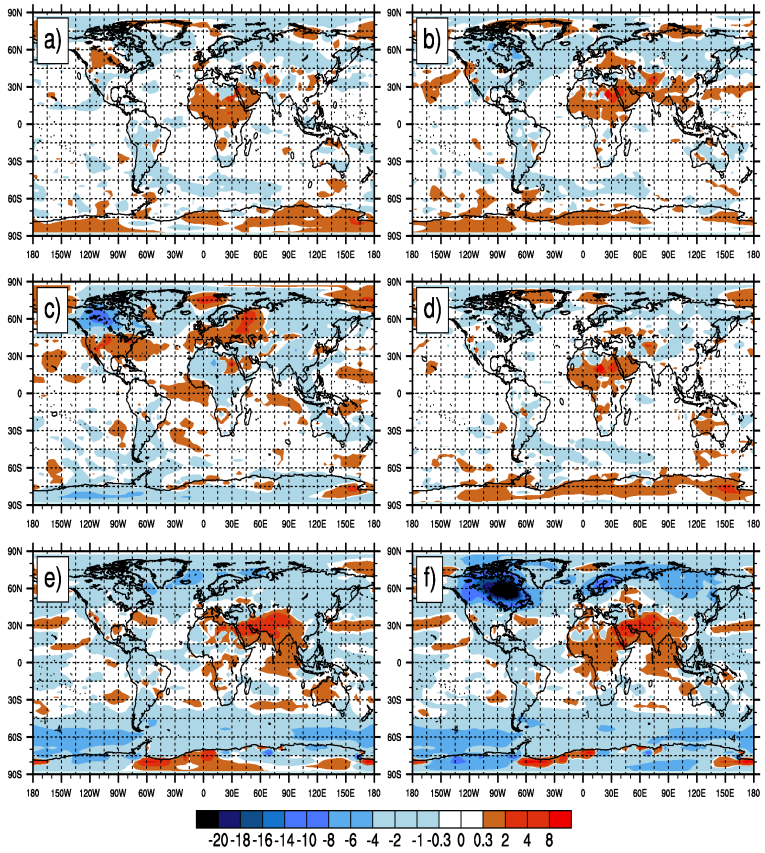


**Fig. 10.** As Fig. 9, but for JJA season.





CPD
8, 1319–1368, 2012



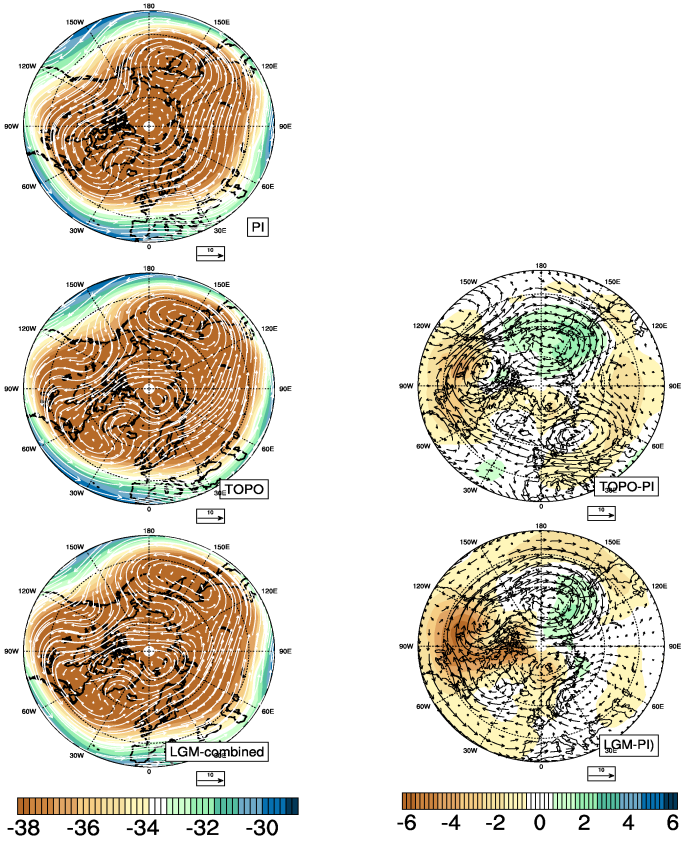


**Fig. 11.** 500 hPa winter (DJF) circulation – left panels: $\delta^{18}O$ (‰) in the vapor and wind vectors ($m\,s^{-1}$) overlaid for the PI, topography and LGM-combined experiments; right panels: the difference of the same from the PI control run.





CPD
8, 1319–1368, 2012



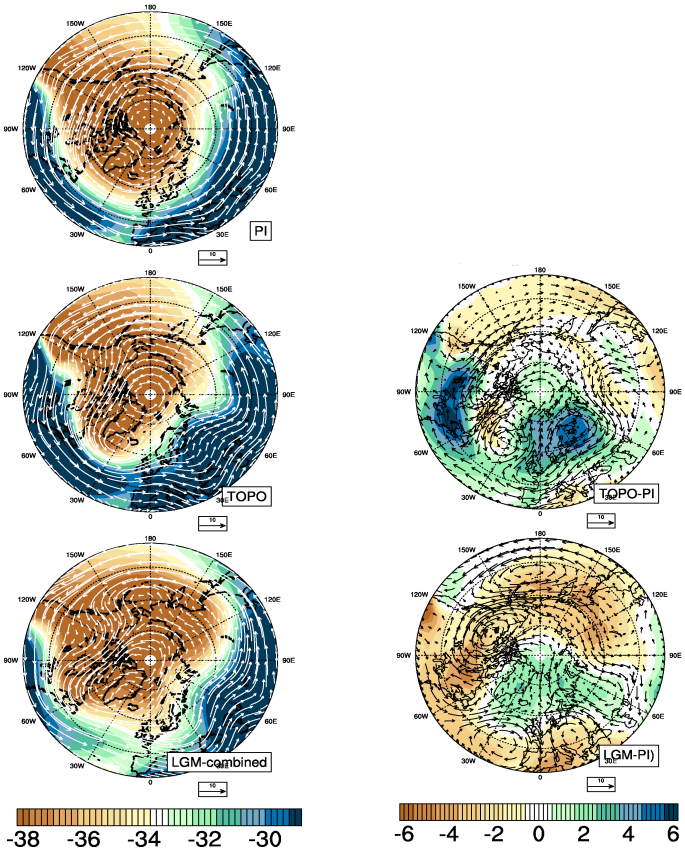


(a) (b)

**Fig. 12.** As Fig. 11, but for JJA season.





CPD
8, 1319–1368, 2012